



High-efficiency and stable syngas production by coupling NiFe-BiVO₄ photoanodes with AgO_x/Ag cathodes

Zhenzhen Zhang ^{a,b}, Xiaojuan Huang ^a, Yingpu Bi ^{a,*}

^a State Key Laboratory for Oxo Synthesis & Selective Oxidation, National Engineering Research Center for Fine Petrochemical Intermediates, Lanzhou Institute of Chemical Physics, CAS, Lanzhou 730000, PR China

^b University of Chinese Academy of Sciences, Beijing 100049, PR China



ARTICLE INFO

Keywords:

Solar energy
BiVO₄
Oxygen evolution
CO₂ reduction
Syngas production

ABSTRACT

Solar-driven photoelectrochemical (PEC) conversion of CO₂ and H₂O into syngas (CO and H₂) provides a promising route for carbon resource utilization. Herein, we demonstrated the integration of BiVO₄-based photoanodes with porous AgO_x/Ag cathodes to construct a highly efficient and stable PEC system for CO₂ conversion into syngas. More specifically, the BiVO₄ photoanode decorated with NiFe cocatalysts enables the highly efficient water oxidation for releasing electron/protons, and porous AgO_x/Ag cathodes with excellent absorption/activation capabilities for CO₂ conversion into syngas. Under simulated sunlight irradiation (AM 1.5 G, 100 mW), a record syngas production activity of 127.1 μmol cm⁻² h⁻¹ (CO/H₂ ratio: ~2: 1) was obtained at 1.23 V vs reversible hydrogen electrode (RHE) accompanying with an excellent durability. A photovoltaic for further utilizing the solar-light (>500 nm) has been integrated to construct a bias-free solar-driven PEC tandem, and the solar-to-syngas conversion efficiency could be achieved up to 4.01%. More importantly, this bias-free PEC CO₂ reduction device could be even operated under weak light-intensity (0.1 sun) and low CO₂ concentration (1.5%), revealing a great potential for practical applications.

1. Introduction

Recent growth of the world economy combined with consumption of fossil fuels have led to rapid increase of carbon dioxide (CO₂) in Earth's atmosphere, which is currently at nearly 421 parts per million (ppm) and significantly accelerates climate change [1–6]. Thereby, the development of new strategies for reducing CO₂ greenhouse gas has become crucial to maintain the global carbon balance [7–9]. Specifically, solar-driven photoelectrochemical (PEC) CO₂ conversion by utilizing water as electron/proton sources to produce syngas (CO and H₂ mixture), a high-priority intermediate for producing commodity chemicals, should be a promising approach [10–12]. According to photoelectrode configurations, the PEC syngas production systems could be basically classified into three categories: photoanode-driven, photocathode-driven, and photoanode-photocathode-driven cells [13]. At present, most of the reported PEC cells for CO₂ conversion are operated with the photocathode-driven mode, while the p-type semiconductor photocathodes usually possess poor structural stability and severe photo-corrosion in aqueous CO₂ solutions [14]. Moreover, a high overpotential is usually required to initiate the anode water oxidation

with sluggish oxygen evolution reaction (OER) kinetics [15]. In contrast, the photoanode-driven PEC cells should be more similar to natural photosynthesis [16], in which water oxidation occurred on light-excited photoanode surfaces at a relatively low potential, and the released electron and proton transferred to cathode surfaces for selective CO₂ reduction into syngas [17]. However, developing high-performance photoanodes is of great fundamental importance for achieving efficient PEC CO₂ conversion owing to the electron/proton participation [18,19]. More specifically, the ideal photoanodes should have an appropriate bandgap (2.0–2.4 eV), favorable band-edge positions, low onset potential, and high charge-carrier mobility, which are all essential for improving PEC water oxidation activities [20,21].

Except for the high performance PEC water oxidation, an efficient cathode catalyst for CO₂ reduction into syngas should be equally important to boost the overall PEC conversion efficiency [22]. Note that CO₂ is a stable and inert molecule with a high symmetry and large C=O bond energy (~750 kJ mol⁻¹), presenting significant challenges toward its chemical absorption/activation [13,22–25]. Recently, it was reported that metal-based catalysts, especially for metallic Ag [26–28], exhibited the relatively high electrocatalytic activities for CO₂ reduction

* Corresponding author.

E-mail address: yingpubi@licp.ac.cn (Y. Bi).

into syngas owing to the suitable binding strength with CO for restraining further reduction to hydrocarbons [29,30]. For example, it was reported demonstrated that Ag nano-catalysts were found to be effective catalysts for electrochemical CO₂-to-CO conversion [31]. Although some progresses have been made in the development of feasible strategies to improve the electrocatalytic activities of metallic Ag catalysts [32], their integration with photoanodes into photoelectrochemical (PEC) devices for CO₂ reduction still remain a great challenge [33]. Specifically, metallic silver catalysts in PEC CO₂ reduction systems is severely affected by low Faraday efficiency and high over-potential [34]. Furthermore, the poor absorption and activation capacity still inhered in the reported Ag-based catalysts [35]. Therefore, rationally tailoring the surface properties of Ag-based cathode catalysts, including atom composition or electronic structure, should be highly desirable for significantly improving the PEC CO₂ reduction activity [36].

In this work, we demonstrated the integration of high-performance BiVO₄ photoanodes with porous AgO_x/Ag catalysts to construct an efficient PEC tandem for syngas production from aqueous CO₂ solution. A record syngas production activity of 127.1 $\mu\text{mol}\cdot\text{cm}^{-2}\cdot\text{h}^{-1}$ (CO/H₂ ratio: ~2:1) has been achieved under simulated sunlight of AM 1.5 G with a relatively high stability. Systematic studies reveal that BiVO₄ photoanode modified with NiFe cocatalysts could enable the highly efficient PEC water oxidation for releasing electron and protons. Simultaneously, the porous AgO_x/Ag cathode catalysts could significantly promote CO₂ absorption and activation capabilities for producing CO and H₂. Further incorporating with a photovoltaic for utilizing the solar-light (>500 nm) to construct a bias-free solar-driven PEC CO₂ reduction device, the solar-to-CO and solar-to-H₂ conversion efficiencies of 2.69 and 1.32% have been achieved, respectively.

2. Experimental section

2.1. Materials and solvents

All chemicals were of analytical grade purity, obtained from Sino-pharm Chemical Reagent Co., Ltd., and used as received without further purification. Deionized water (Molecular Corp., 18.25 MΩ cm) used in the synthesis was from local sources. Bismuth nitrate pentahydrate (Bi (NO₃)₃·5 H₂O, 99%), potassium iodide (KI, 98.5%), 1,4-Benzoquinone (C₁₂H₁₀O₄), vanadium acetylacetone oxygen (VO(acac)₂), dimethylsulfoxide (DMSO), sodium hydroxide (NaOH, 99%), ethyl alcohol, iron chloride hexahydrate (FeCl₃·6 H₂O, 99%), nickel chloride hexahydrate (NiCl₂·6 H₂O, 99%), Sodium hypophosphite monohydrate (NaH₂PO₂·H₂O, AR), potassium bicarbonate (KHCO₃), Deionized water (Molecular Corp., 18.25 MΩ cm) used in the synthesis was from local sources. All reagents were analytical grade and used without further purification.

2.2. Preparation of nanoporous BiVO₄ photoanode

Porous BiVO₄ photoanodes supported fluorine-doped tin-oxide (FTO) glass were synthesized according to the literature previous report [37]. The nanoporous BiVO₄ photoanodes are firstly prepared by electrodeposition combined with high temperature calcination, followed by the loading of FeNiOOH onto the BiVO₄ surface by impregnation and finally calcination in a tube furnace equipped with NaH₂PO₂·H₂O to obtain high performance and stable BiVO₄-based photoanodes.

2.3. Preparation of AgO_x/Ag nanostructure cathodes

The porous AgO_x/Ag nanostructures were prepared by a modified plasma and electroreduction treatment.^[40] First, the Ag foil is polished and cleaned (99.999%, 10 × 15 × 0.2 mm) and then treated on both sides for 30 min in O₂ plasma (20 Pa, 6.8 W). The silver foil with a black surface is then activated using electrochemical reduction

(-0.3–1 V_{vs}AgCl/Ag), rinsed several times with deionised water to remove any possible impurities on the surface and dried to give an AgO_x/Ag cathode.

2.4. Photoelectrochemical CO₂ reduction with three-electrode system

The photoelectrochemical CO₂ reduction was performed in an H cell with a proton-exchange membrane (Nafion 115) separating the anode and cathode, and the electrolyte used in this work was 1 M KHCO₃ and 0.5 M K₃BO₃ for cathode and anode, respectively. In a typical artificial photosynthesis system, BiVO₄ film and saturated Ag/AgCl were used as the working electrode and reference electrode in the anode cell, respectively, and the prepared AgO_x/Ag was used as the counter electrode in the cathode cell. For photosynthesis, the working electrode was placed under simulated sunlight irradiation (100 mW·cm⁻²) with different bias voltage, while the cathodic cell was placed in dark conditions. Before the reaction procedure, the cathode solution was saturated by continuous bubbling with CO₂ gas. During the reaction, the gas composition of the cathode cell was analyzed by Shimadzu GC-2014 C gas chromatography equipped with a Ni conversion furnace (TCD and FID, 5 A molecular sieve and TDX-1 columns). The CO₂ reduction cycling test was performed at 1.23 V_{RHE} with a BiVO₄ photoanode as the working electrode under the simulated solar irradiation and an AgO_x/Ag film as the cathode under the dark conditions. The electrolytes of the anode and cathode cells were 0.5 M K₃BO₃ and CO₂-saturated 1 M KHCO₃ solution, respectively. After one hour of single cycle test, the gas in the cathode cell was detected by the GC, and the electrolyte solution was refilled for the next cycle test. The ¹³C labeled isotope tracer experiment was performed and the products were analyzed by a gas chromatography-mass spectrometry (GC-MS, 7890 A and 5975 C, Agilent).

2.5. Solar-driven photoelectrochemical CO₂ reduction

Photochemical CO₂ reduction without additional bias was tested in a two-electrode system. First AgO_x/Ag is placed in a 1 M KHCO₃ cathode cell and the BiVO₄ photoanode is illuminated in a 0.5 M K₃BO₃ electrolyte. As the BiVO₄ photoanode can only absorb light <500 nm, we fully utilize light from the solar spectrum (>500 nm) that is not available to the photoanode by means of a polycrystalline silicon solar panel. A long-pass filter (RG-510, Edmund Optics) is therefore added to the light outlet of another light source (AM 1.5 G) to provide light at >500 nm. This long wavelength light irradiates an 80 × 60 mm polycrystalline solar cell with a maximum open circuit voltage of 1.5 V to provide the voltage to drive the entire system, where the total power irradiated on the solar cell is controlled at 76.7 mW (calculated from the AM 1.5 G spectrum). The light power irradiated on the photoanode and solar cell was also scaled to test the effect of different light intensities (0.1, 0.3, 0.5, 0.7 and 1 sun) on the photochemical CO₂ reduction. The different photovoltaic voltages were achieved by changing solar cells with various open circuit voltage.

2.6. Characterizations

Transmission electron microscopy (TEM) measurements were performed by using an FEI Tecnai TF20 microscope operated at 200 kV. Scanning electron microscopy measurements were carried out on a field-emission scanning electron microscope (SEM, JSM-6701 F, JEOL) operated at an accelerating voltage of 5 kV. UV-visible diffuse reflectance spectra were obtained on a UV-2550 (Shimadzu) spectrometer by using BaSO₄ as the reference. Raman spectra (LabRAM HR Evolution) were obtained to probe the local structure with red (785 nm) and green (532 nm) lasers. The elemental composition and chemical valence states were determined by X-ray photoelectron spectroscopy (XPS, ESCALAB 250Xi). The crystalline structure of the samples was identified by X-ray diffraction analysis (XRD, X' Pert PRO) using Cu K α radiation with

scanning rates of $0.06^\circ/\text{min}$ and 0.001° per step and voltages and currents of 50 kV and 50 mA . The Atomic force microscope (AFM) images were collected on Icon 2-SYS (Bruker). Temperature-programmed desorption profiles of CO_2 or CO (CO_2 -TPD or CO -TPD) were obtained on a chemical adsorption instrument (Micromeritics, ChemiSorb 2720). Before the adsorbed CO_2 molecules were desorbed under a purge of $25 \text{ mL}\cdot\text{min}^{-1}$ of helium with a heating rate of $10 \text{ }^\circ\text{C}/\text{min}$, the samples were saturated with CO_2 at $25 \text{ }^\circ\text{C}$. The in-situ FT-IR of CO_2 adsorption was carried out in a mixed atmosphere of CO_2 and H_2O vapor by a Fourier transform infrared spectroscopy (VERTEX 70, Bruker) with a sealed sample chamber (Harrick).

3. Results and discussions

The BiVO_4 -based photoanodes were prepared by a facile electrochemical deposition followed with the calcination treatment, which were subsequently decorated with NiFe OER catalysts by a phosphating strategy (Figure S1). Additionally, a nanoporous AgO_x/Ag cathode catalyst was synthesized by treating commercial Ag foils with the combination of oxygen-plasma with electrochemical treatments. The surface structure and morphology of obtained AgO_x/Ag cathodes were explored by field emission scanning electron microscopy (FE-SEM). As shown in Fig. 1 A, the typical top-view FE-SEM images clearly demonstrated that the obtained AgO_x/Ag cathodes possess a nanoporous structure with an average diameter of $200\text{--}300 \text{ nm}$. Additionally, the transmission electron microscopy (TEM) image of AgO_x/Ag cathodes shown in Fig. 1B further reveals their porous structure. The energy dispersive spectroscopy (EDS) analysis has performed to validate the elemental composition (insert in Fig. 1B). Both elemental mapping and line-scan results clearly show that Ag and O elements are uniformly distributed on the whole detection regions. The high-resolution TEM (HR-TEM) images (Fig. 1 C and Figure S3) demonstrated that an obvious lattice fringe of 0.236 nm could be indexed to (111) plane of metallic Ag. Interestingly, a uniform amorphous ultrathin layer with a thickness of $\sim 2 \text{ nm}$ was clearly observed on Ag particle surfaces, which should be attributed to the formation of AgO_x nanolayers. Fig. 1D shows the X-ray

diffraction (XRD) patterns of both metallic Ag foils and AgO_x/Ag samples, revealing that all the diffraction peaks could be indexed to the face-centered cubic structure of silver phase (JCPDS No. 89-3722), while no diffraction peaks corresponding to AgO_x species could be detected, mainly resulting from their amorphous structure and ultrathin thickness. In addition, Fig. 1E shows the Raman spectra of both Ag foils and AgO_x/Ag catalysts. Compared with pristine Ag foils, the new Ag-O peaks around 685 , 985 and 1052 cm^{-1} could be evidently detected in AgO_x/Ag samples, further confirming the formation of AgO_x nanolayers on Ag particle surfaces [37]. The X-ray photoelectron spectroscopy (XPS) valence band (VB) has also been measured to explore the surface chemical states. As shown Fig. 1 F, the significant changes between Ag foil and AgO_x/Ag samples clearly demonstrate the formation of AgO_x nanolayers on porous Ag surfaces after oxygen-plasma and electrochemical treatments, which could be further confirmed by the XPS spectra and Ag MNN Auger spectra (Figure S7 and S8).

The fabricated AgO_x/Ag cathodes were integrated with BiVO_4 photoanodes to construct a PEC CO_2 reduction tandem separated by proton exchange membrane, and the schematic diagram has been shown in Fig. 2 A. The BiVO_4 photoanodes were irradiated under AM 1.5 G simulated sunlight ($100 \text{ mW}/\text{cm}^2$) to initiate the PEC CO_2 reduction to syngas. The linear sweep voltammetry (LSV) curves shown in Fig. 2B clearly reveal that the $\text{BiVO}_4\text{-AgO}_x/\text{Ag}$ tandem exhibits an outstanding photocurrent density of 6.73 mA cm^{-2} at $1.23 \text{ V}_{\text{RHE}}$, accompanying by a lower onset potential ($0.3 \text{ V}_{\text{RHE}}$). However, when light-irradiation on BiVO_4 photoanodes was removed, no evident photocurrent could be detected in the whole potential ranges ($0.2\text{--}1.6 \text{ V}_{\text{RHE}}$). Furthermore, when BiVO_4 photoanodes were replaced by commercial Pt electrodes to construct an electrocatalytic Pt- AgO_x/Ag system, no evident current for CO_2 reduction could be observed. Thereby, these demonstrations clearly reveal that the $\text{BiVO}_4\text{-AgO}_x/\text{Ag}$ tandem for driving PEC CO_2 reduction should be initiated by light-excited BiVO_4 photoanodes. Except for the excellent PEC activity, the high stabilities are equivalently required towards future practical application. Fig. 2 C shows the related current-time (i-t) curves measured at $1.23 \text{ V}_{\text{RHE}}$, and the photocurrent density of $\text{BiVO}_4\text{-AgO}_x/\text{Ag}$ tandems could well maintain constant during

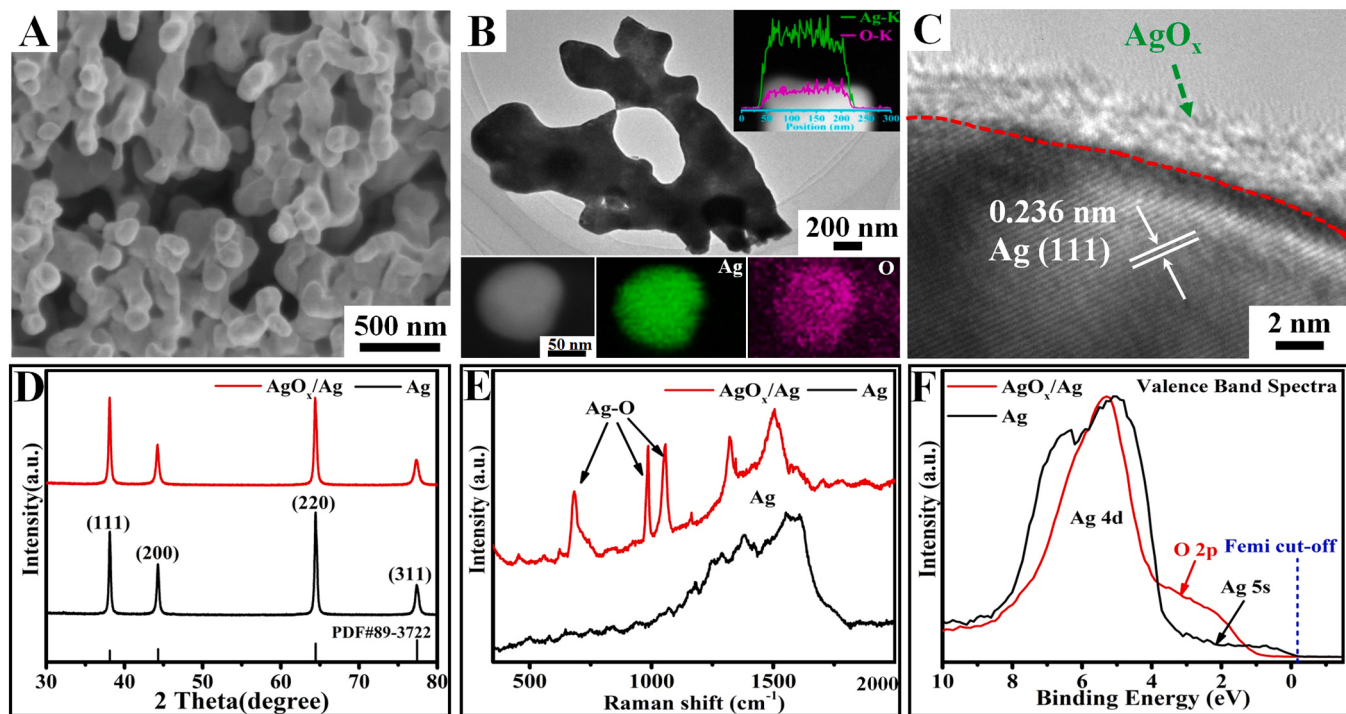


Fig. 1. (A) SEM, (B) TEM, and (C) HR-TEM images of AgO_x/Ag cathode catalyst, Inset of (B): the EDS mapping images and TEM-EDS line analysis; (D) XRD pattern, (E) Raman spectra and (F) Valence band spectra of Ag and AgO_x/Ag cathode catalysts.

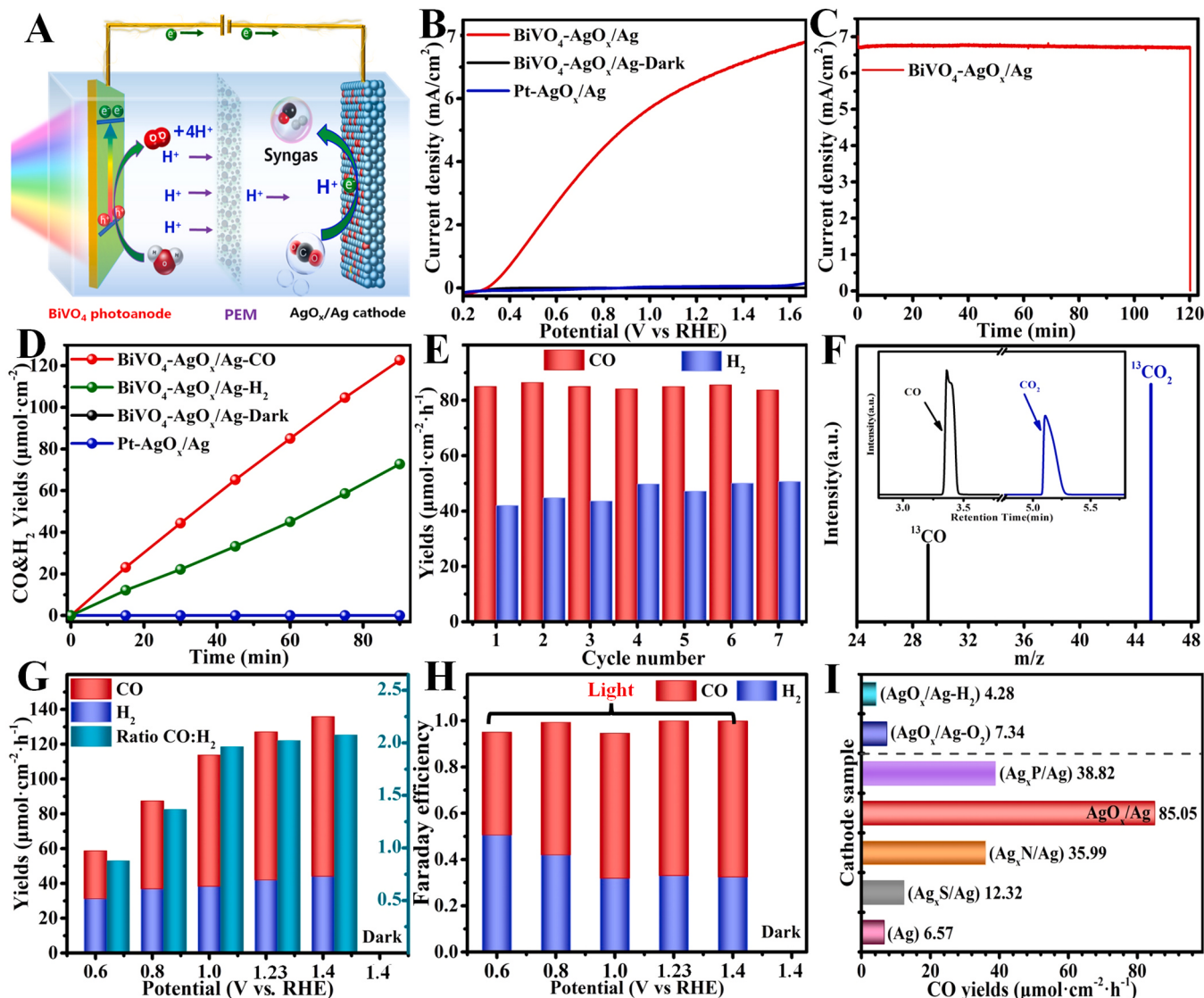


Fig. 2. (A) Schematic diagram of BiVO₄-AgO_x/Ag tandems for syngas production, (B) LSV curves of BiVO₄-AgO_x/Ag and Pt-AgO_x/Ag tandems, (C) PEC stability test of BiVO₄-AgO_x/Ag, (D) CO and H₂ evolution amounts of BiVO₄-AgO_x/Ag and Pt-AgO_x/Ag tandems at 1.23 V_{RHE}, (E) CO/H₂ yields during cycling tests, (F) GC-MS product analysis using ¹³CO₂ as the carbon source, (G) CO/H₂ yields and ratio, (H) Faraday efficiencies of BiVO₄-AgO_x/Ag tandems at different voltages, (I) CO yields by integrating BiVO₄ photoanodes with different cathodes.

120 min light-irradiation, indicating their relatively high structure-stabilities for PEC CO₂ reduction.

The CO₂ reduction products in this BiVO₄-AgO_x/Ag tandem were analyzed by gas chromatography, and evident CO and H₂ peaks could be detected (Figure S9). As shown in Fig. 2D, the CO and H₂ amounts have been linearly increased with extending light irradiation time, which could be reached up to 120.05 and 72.04 μmol cm⁻² after 1.5 h test, respectively. However, no any CO or H₂ could be produced when the light irradiation was removed from BiVO₄ photoanode or replaced with Pt electrode, confirming that water oxidation for releasing electron/proton on BiVO₄ photoanode should be crucial to initiate cathode CO₂ reduction for syngas production. The cycle stability of this BiVO₄-AgO_x/Ag tandem for syngas production was further explored and shown in Fig. 2E, revealing that both CO and H₂ evolution activities could well keep constant during the whole cycle tests, confirming the relatively high stability for converting aqueous CO₂ solutions into syngas. Furthermore, ¹³C-labeled isotope tracer experiment was conducted to explore the source of CO products. As shown in Fig. 2F, by using the isotopically labeled ¹³CO₂ as reaction gas, the evident signal peaks at *m/z*=45.1 (¹³CO₂) and *m/z*=29.1 (¹³CO) in the mass spectrometer (MS)

have been detected, confirming that the CO product should be derived from CO₂ rather than the electrolyte or other impurities. In addition, the CO: H₂ ratios in the obtained syngas could be reasonably adjusted from 0.88 to 2.08 by changing the potential (Fig. 2G), and their Faraday efficiencies for the syngas production were all above 95% (Fig. 2H). To further confirm the high activity and selectivity of AgO_x/Ag cathodes for syngas production, BiVO₄ photoanodes integrated with other cathode catalysts have also been explored under the same conditions. As shown in Fig. 2I, the CO production rates of pristine Ag foils, Ag_xS/Ag, Ag_xN/Ag, and Ag_xP/Ag catalysts are 6.57, 12.32, 35.99, and 38.82 μmol·cm⁻²·h⁻¹, respectively, which are all much lower than that of AgO_x/Ag catalysts (85.05 μmol·cm⁻²·h⁻¹). Furthermore, when reduction or oxidation treatments were performed on AgO_x/Ag catalysts to form metallic Ag and Ag₂O (marked as AgO_x/Ag-H₂ and AgO_x/Ag-O₂, Figure S10), CO production rates have been significantly decreased down to 4.28 and 7.34 μmol·cm⁻²·h⁻¹, respectively (Figure S11). These demonstrations clearly reveal that the ultrathin AgO_x nanolayers on the Ag surface should play a crucial role in determining the catalytic activity and selectivity for CO₂ reduction reaction.

To further explore the possible CO₂ reduction mechanisms, the

surface composition and chemical states of AgO_x/Ag cathode catalysts before and after CO_2 adsorption have been studied by a quasi in-situ XPS technique. Note that the AgO_x/Ag cathodes were preliminarily cleaned by a low-energy Ar plasma treatment to remove the surface contaminants. As shown in Fig. 3 A, an evident shoulder peak at low binding energy (BE) positions could be observed in $\text{Ag}\ 3\text{d}$ peaks of AgO_x/Ag cathodes, which should be attributed to the formation of ultrathin AgO_x nanolayers on the Ag surface. Amazingly, this shoulder peak completely disappear after CO_2 adsorption on AgO_x/Ag surfaces, while no obvious changes of Ag 3d peaks could be detected on pristine Ag foil surfaces (Figure S15). Moreover, the C 1s peaks (Fig. 3B) clearly reveal that before CO_2 absorption, only trace HCO_3^- and C-C peaks could be identified on AgO_x/Ag surfaces. The evident $\text{O}=\text{C}-\text{O}$ and $\text{O}=\text{C}=\text{O}$ peaks at 285.5 and 288.5 eV could be observed after CO_2 absorption, which should be attributed to CO_2 chemical adsorption and activation on AgO_x/Ag surfaces. Furthermore, the VB spectrum changes of AgO_x/Ag cathode has been studied and compared in Fig. 3 C. It can be observed that the CO_2 adsorption on AgO_x/Ag cathode induced the transformation of surface AgO_x layers into metallic Ag.

To further confirm the above speculations, the temperature-programmed desorption (TPD) of CO_2 have been conducted to explore the CO_2 adsorption and activation on the surface of AgO_x/Ag [38]. As shown in Fig. 3D, a relatively broad desorption peak with a low intensity on the pristine Ag foils could be observed compared to the strong desorption peaks around 400–600°C on AgO_x/Ag samples, indicating

the excellent chemisorption capability of CO_2 molecules on AgO_x/Ag cathode than pristine Ag foils. Furthermore, the CO-TPD results (Figure S16) and XPS results (Figure S17) clearly indicate that AgO_x/Ag demonstrated a relatively weak ability to interact with CO compared to pristine Ag, which could facilitate effective desorption of CO molecules from the cathode surface (Figure S18). The in-situ Fourier transform infrared reflection (FTIR) spectra of CO_2 adsorption and activation on AgO_x/Ag cathode has been shown in Fig. 3E and Figure S19, indicating that the absorption peaks at $\sim 2350\text{ cm}^{-1}$ corresponding to the stretching vibration of CO_2 molecules is significantly increased compared with the bending vibration ($\sim 670\text{ cm}^{-1}$). The results confirming that the AgO_x/Ag surfaces should be more effective for promoting the CO_2 activation. On the basis of above results, it may be proposed that the Ag^{n+} species on AgO_x nanolayers should serve as active sites for CO_2 absorption and activation (Fig. 3 F). More specifically, the CO_2 absorption would donate electrons to Ag^{n+} active sites of AgO_x/Ag cathode to form Ag^0 . In addition, the $\text{O}=\text{C}=\text{O}$ bond of CO_2 would be broken to form $\text{O}=\text{C}-\text{O}$ and $^*\text{COOH}$ intermediates (Figure S20), owing to the electron and proton transferred from BiVO_4 photoanodes. In addition, Figure S21 shows the contact angles of Ag and AgO_x/Ag surfaces with water, revealing that the hydrophilicity of AgO_x/Ag surfaces is much higher than that of pristine Ag. Furthermore, the water molecules could further enhance the CO_2 absorption and activation on AgO_x/Ag cathode surface (Figure S22). Thereby, the selective CO_2 reduction to CO on AgO_x/Ag cathode surfaces has been

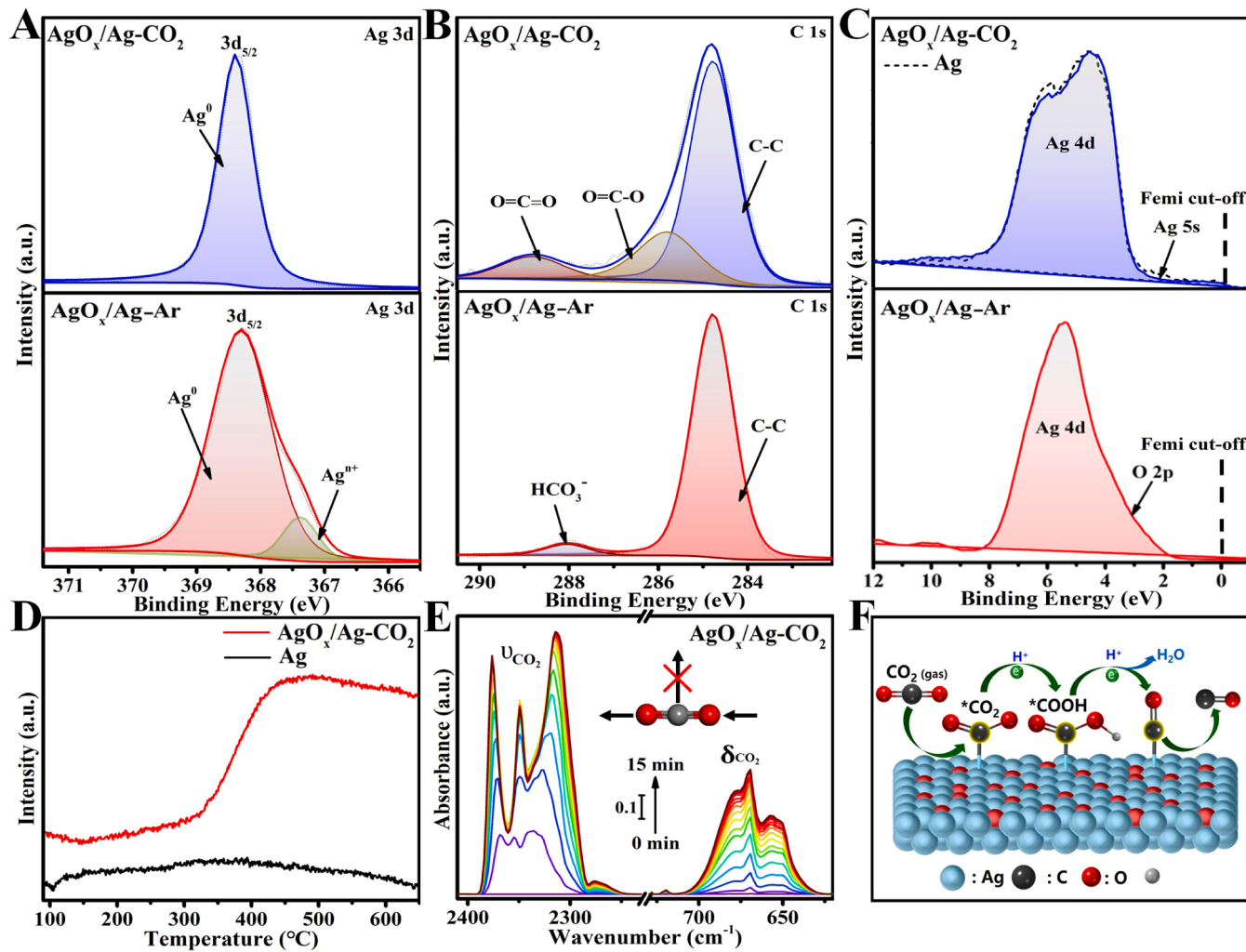


Fig. 3. (A) Ag 3d, (B) C 1s XPS spectra and (C) Valence band spectrum of cleaned AgO_x/Ag alloy films before and after CO_2 adsorption. (D) CO_2 -TPD and (E) in-situ FTIR spectra of CO_2 desorption and adsorption for Ag and AgO_x/Ag . (F) Schematic diagrams illustrating the CO_2 reduction on AgO_x/Ag cathode surfaces.

achieved accompanying with H_2O formation.

In order to further make full use of sunlight, a polycrystal silicon solar cell is assembled with this $\text{BiVO}_4\text{-AgO}_x\text{/Ag}$ tandem to construct an overall solar-driven PV-PEC CO_2 reduction device, in which BiVO_4 photoanodes absorb light wavelength below 500 nm and polycrystal silicon absorb light above 500 nm (inset of Fig. 4 A). The photocurrent density of this PV-PEC system could be reached up to $3.09 \text{ mA}\cdot\text{cm}^{-2}$ under light irradiation (AM 1.5 G, 1 sun intensity) accompanying with an excellent stability during the measurement of 10 h. As shown in Fig. 4B, when the light-irradiation on BiVO_4 photoanode was removed, the photocurrent rapidly dropped to near zero. Additionally, no CO or H_2 products could be detected in the PV-EC device (Fig. 4 C). These results clearly reveal that this PV-PEC CO_2 reduction device for syngas production is driven by the BiVO_4 photoanode rather than the solar cell. Furthermore, the amount of CO and H_2 from this solar-driven PEC CO_2 reduction device could be reached up to 37.64 and $20.09 \mu\text{mol}$, respectively. The total solar-to-fuel (STF) conversion efficiency was calculated to be 4.01%, and the solar-to- CO and solar-to- H_2 conversion efficiencies were 2.69% and 1.32%, respectively. In addition, Fig. 4D and Figure S23 shows the effects of light intensity on the activity and selectivity of CO_2 reduction, indicating that this PEC device could convert CO_2 into syngas even at 0.1 sunlight intensity. The effect of solar cell voltage was also explored (Fig. 4E). Interestingly, CO and H_2 could be even detected at 0.5 V, indicating that low voltage could also drive the PEC system. With increasing voltages, the optimal activity and selectivity for CO production was 1.5 V, indicating that the voltages play an important role in determining the CO : H_2 ratios in the syngas products. Furthermore, this solar-driven device could also be operated in a low concentration (1.5%) of CO_2 atmosphere for syngas production (Fig. 4 F). All these demonstrations clearly indicate that this solar-driven PV-PEC CO_2 reduction device possess a great potential for practical application owing to its high adaptability. In addition, Figure S24 and Table S1 summarized the reported STF conversion efficiencies for unbiased PEC CO_2 reduction in recent years, and a record solar conversion

efficiency has been achieved in this BiVO_4 photoanode-driven system.

4. Conclusion

In summary, we have demonstrated a facile strategy to rationally fabricate the porous $\text{AgO}_x\text{/Ag}$ cathode catalysts, which were integrated with a high performance BiVO_4 photoanodes to construct a solar-driven PEC tandem for syngas production from aqueous CO_2 solution. Owing to the synergistic effects of BiVO_4 photoanodes for highly efficient PEC water oxidation and porous $\text{AgO}_x\text{/Ag}$ cathode catalysts with excellent CO_2 absorption/activation capability, a record syngas production activity of $127.1 \mu\text{mol}\cdot\text{cm}^{-2}\cdot\text{h}^{-1}$ (CO/H_2 ratio: ~2:1) has been achieved under simulated sunlight. Additionally, the ratio of CO to H_2 in the PEC syngas products could be rationally tailored by adjusting bias potentials. A photovoltaic has also been further integrated with this PEC tandem to achieve the bias-free solar-driven syngas production, which could obtain a solar-to-syngas conversion efficiency of 4.01% as well as an excellent durability. Thereby, this work provides a promising strategy for achieving efficient solar-driven PEC syngas production from aqueous CO_2 solutions.

CRediT authorship contribution statement

Yingpu Bi: Writing – review & editing, Supervision, Conceptualization. **Xiaojuan Huang:** Investigation. **Zhenzhen Zhang:** Writing – original draft, Investigation.

Declaration of Competing Interest

The authors declare that they have no known competing financial interests or personal relationships that could have appeared to influence the work reported in this paper.

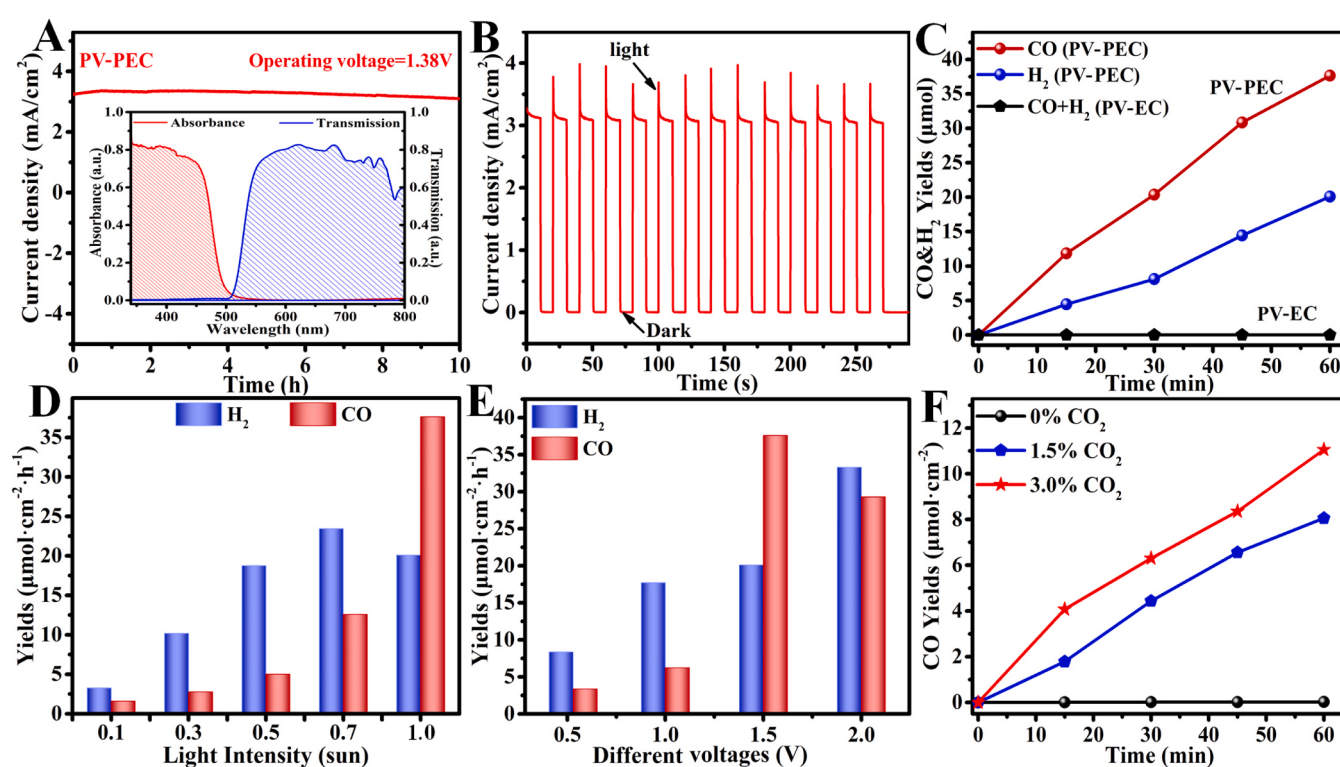


Fig. 4. (A) i - t stability test (Inset: absorption and transmission spectra of the BiVO_4 photoanode and solar cell cut-off filter, respectively), (B) i - t curves of chopped irradiation for PV-PEC, (C) syngas production amounts under 1 sun irradiation, (D) and (E) syngas amounts and CO : H_2 ratios under different light intensities and different voltages, respectively, (F) syngas amounts of the CO_2 reduction process under unsaturated CO_2 solutions.

Data availability

Data will be made available on request.

Acknowledgments

The work was supported by the National Natural Science Foundation of China (21832005, 22072168, 22002175), Major Program of the Lanzhou Institute of Chemical Physics, CAS (No. ZYFZFX-3), Major Science and Technology Projects in Gansu Province (22ZD6GA003), and the CAS “Light of West China” Program and West Light Foundation of The Chinese Academy of Sciences (xbzg-zdsys-202209).

Appendix A. Supporting information

Supplementary data associated with this article can be found in the online version at [doi:10.1016/j.apcatb.2024.123894](https://doi.org/10.1016/j.apcatb.2024.123894).

References

- [1] K. Ye, G.R. Zhang, X.Y. Ma, C.W. Deng, X. Huang, C.H. Yuan, G. Meng, W.B. Cai, K. Jiang, *Energy Environ. Sci.* 15 (2022) 749–759.
- [2] Z. Sun, T. Ma, H. Tao, Q. Fan, B. Han, *Chem* 3 (2017) 560–587.
- [3] T.A. Kistler, M.Y. Um, J.K. Cooper, I.D. Sharp, P. Agbo, *Adv. Energy Mater.* 11 (2021) 2100070.
- [4] B. Tang, F.-X. Xiao, *ACS Catal.* 12 (2022) 9023–9057.
- [5] X.H. Liu, Y.C. Deng, L.R. Zheng, M.R. Kesama, C. Tang, Y.F. Zhu, *ACS Catal.* 12 (2022) 5517–5526.
- [6] Z.H. Mou, R.X. Yan, J. Peng, Y. Li, Z.Y. Huang, Z.J. Wang, B. Zhao, D. Xiao, *Chem. Eng. J.* 465 (2023) 142986.
- [7] V. Andrei, R.A. Jagt, M. Rahaman, L. Lari, V.K. Lazarov, J.L.M. Driscoll, R.L. Z. Hoye, E. Reisner, *Nat. Mater.* 21 (2022) 864–868.
- [8] Y. Zhang, D.L. Pan, Y. Tao, H. Shang, D.Q. Zhang, G.S. Li, H.X. Li, *Adv. Funct. Mater.* 32 (2021) 2109600.
- [9] E.E. Moore, V. Andrei, A.R. Oliveira, A.M. Coito, I.A.C. Pereira, E. Reisner, *Angew. Chem. Int. Ed.* 60 (2021) 26303–26307.
- [10] H. Xiang, H.A. Miller, M. Bellini, H. Christensen, K. Scott, S. Rasul, E.H. Yu, *Sustain. Energy Fuels* 4 (2020) 277–284.
- [11] C. Pornrungroj, V. Andrei, M. Rahaman, C. Uswachoke, H.J. Joyce, D.S. Wright, E. Reisner, *Adv. Funct. Mater.* 31 (2020) 2008182.
- [12] J.T. Song, H. Ryoo, M. Cho, J. Kim, J.G. Kim, S.Y. Chung, J.H. Oh, *Adv. Energy Mater.* 7 (2017) 1601103.
- [13] Y. Zou, S. Wang, *Adv. Sci.* 8 (2021) 2003579.
- [14] Y. Liu, Y. Zou, W. Zhao, M. Wang, C. Li, S. Liu, S.Y. Wang, *Nano Sel.* 1 (2020) 135–151.
- [15] B. Liu, X. Wang, Y.J. Zhang, L.C. Xu, T.S. Wang, X. Xiao, S.C. Wang, L.Z. Wang, W. Huang, *Angew. Chem. Int. Ed.* 62 (2023) e202217346.
- [16] B. Zhao, X. Huang, Y. Ding, Y. Bi, *Angew. Chem. Int. Ed.* 62 (2023) e202213067.
- [17] W. Tu, Y. Zhou, Z. Zou, *Adv. Mater.* 26 (2014) 4607–4626.
- [18] B. Han, J.X. Wang, C.X. Yan, Y.P. Dong, Y.J. Xu, R. Nie, H.Y. Jing, *Electrochim. Acta* 285 (2018) 23–29.
- [19] D.W. Huang, K. Wang, L.T. Li, K. Feng, N. An, S. Ikeda, Y.B. Kuang, Y.H. Ng, F. Jiang, *Energy Environ. Sci.* 14 (2021) 1480–1489.
- [20] Y. Zhao, C.M. Ding, J. Zhu, W. Qin, X.P. Tao, F.T. Fan, R.G. Li, C. Li, *Angew. Chem. Int. Ed.* 59 (2020) 9653–9658.
- [21] Y. Qi, J.W. Zhang, Y. Kong, Y. Zhao, S. Chen, D. Li, W. Li, Y.F. Chen, T.F. Xie, J. Y. Cui, C. Li, K. Domen, F.X. Zhang, *Nat. Commun.* 13 (2022) 484.
- [22] V. Andrei, B. Reuillard, E. Reisner, *Nat. Mater.* 19 (2020) 189–194.
- [23] M.B. Ross, P.D. Luma, Y.F. Li, C.T. Dinh, D. Kim, P.D. Yang, E.H. Sargent, *Nat. Catal.* 2 (2019) 648–658.
- [24] Y.J. Jang, M.D. Bhatt, J. Lee, S.H. Choi, B.J. Lee, J.S. Lee, *Adv. Energy Mater.* 8 (2018) 1702636.
- [25] Z. Mou, J. Peng, R. Yan, Q. Yang, B. Zhao, D. Xiao, *Carbon* 203 (2023) 11–20.
- [26] Q. Lu, J. Rosen, Y. Zhou, G.S. Hutchings, Y.C. Kimmel, J.G.C. Chen, F. Jiao, *Nat. Commun.* 5 (2014) 3242.
- [27] Y. Yoon, A.S. Hall, Y. Surendranath, *Angew. Chem. Int. Ed.* 55 (2016) 15282–15286.
- [28] N.Q. Zhang, X.X. Zhang, L. Tao, P. Jiang, C.L. Ye, R. Lin, Z.W. Huang, A. Li, D. W. Pang, H. Yan, Y. Wang, P. Xu, S.F. An, Q.H. Zhang, L.C. Liu, S.X. Du, X.D. Han, D.S. Wang, Y.D. Li, *Angew. Chem. Int. Ed.* 60 (2021) 6170–6176.
- [29] Y.C. Hsieh, S.D. Senanayake, Y. Zhang, W. Xu, D.E. Polyansky, *ACS Catal.* 5 (2015) 5349–5356.
- [30] Y.S. Ham, S. Choe, M.J. Kim, T. Lim, S.K. Kim, J.J. Kim, *Appl. Catal. B* 208 (2017) 35–43.
- [31] C. Kim, H.S. Jeon, T. Eom, M.S. Jee, H. Kim, C.M. Friend, B.K. Min, Y.J. Hwang, *J. Am. Chem. Soc.* 137 (2015) 13844–13850.
- [32] D. Ma, Y.R. Ying, K. Zhang, Y.L. Gao, L.J. Zhou, A. Song, Y.P. Zhou, K.Y. Xie, T. Jin, H.T. Huang, *Appl. Catal. B* 316 (2022) 121658.
- [33] S.M. Lee, H. Lee, J. Kim, S.H. Ahn, S.T. Chang, *Appl. Catal. B* 259 (2019) 118045.
- [34] L.Q. Ye, J.Y. Liu, C.Q. Gong, L.H. Tian, T.Y. Peng, L. Zan, *ACS Catal.* 2 (2012) 1677–1683.
- [35] Z. Zhao, J. Zhang, M. Lei, Y. Lum, *Nano Res. Energy* 2 (2023) e9120044.
- [36] H. Mistry, Y.W. Choi, A. Bagger, F. Scholten, C.S. Bonifacio, I. Sinev, N.J. Divins, L. Zegkinoglou, H.S. Jeon, K. Kisslinger, E.A. Stach, J.C. Yang, J. Rossmeisl, B. R. Cuanya, *Angew. Chem. Int. Ed.* 56 (2017) 11394–11398.
- [37] X.Y. Wang, J. Yang, L. Zhou, G. Song, F. Lu, L.J. You, J.Y. Li, *Colloids Surf. A Physicochem. Eng. Asp.* 610 (2021) 125414.
- [38] K.K. Bando, K. Sayama, H. Kusama, K. Okabe, H. Arakawa, *Appl. Catal. A-Gen.* 165 (1997) 391–409.